An Embedded-Sensor Approach for Concrete Resistivity Measurement in On-Site Corrosion Monitoring: Cell Constants Determination

Jose Enrique Ramón [1,*], Isabel Martínez [1], José Manuel Gandía-Romero [2] and Juan Soto [3]

[1] Instituto de Ciencias de la Construcción Eduardo Torroja, CSIC, C/Serrano Galvache No.4, 28033 Madrid, Spain; isabel.martinez@csic.es

[2] Department of Architectural Construction, Universitat Politècnica de València, Camino de Vera s/n, 46022 Valencia, Spain; joganro@csa.upv.es

[3] Interuniversity Research Institute for Molecular Recognition and Technological Development, Universitat Politècnica de València—Universitat de València, Camino de Vera s/n, 46022 Valencia, Spain; juan-soto@qim.upv.es

* Correspondence: jose.ramon@ietcc.csic.es

Abstract: The concrete electrical resistivity is a prominent parameter in structural health monitoring, since, along with corrosion potential, it provides relevant qualitative diagnosis of the reinforcement corrosion. This study proposes a simple expression to reliable determine resistivity from the concrete electrical resistance (R_E) provided by the corrosion sensor of the Integrated Network of Sensors for Smart Corrosion Monitoring (INESSCOM) we have developed. The novelty here is that distinct from common resistivity sensors, the cell constants obtained by the proposed expression are intended to be valid for any sensor implementation scenario. This was ensured by studying most significant geometrical features of the sensor in a wide set of calibration solutions. This embedded-sensor approach is intended to be applicable for R_E measurements obtained both using potential step voltammetry (PSV, used in the INESSCOM sensor for corrosion rate measurement) and alternating current methods. In this regard, we present a simple protocol to reliably determine R_E, and therefore resistivity, from PSV measurements. It consists in adding a very short potentiostatic pulse to the original technique. In this way, we are able to easy monitor resistivity along with corrosion rate through a single sensor, an advantage which is not usual in structural health monitoring.

Keywords: structure health monitoring; resistivity; sensor; non-destructive technique; steel corrosion; reinforced concrete; durability

1. Introduction

The service life of reinforced concrete structures depends largely on the extent of reinforcement corrosion, known to begin when certain aggressive agents such as CO_2 and chloride ions come into contact with and destroy the passive film formed on the steel rebars [1]. Hence the importance of concrete cover quality, for it is the sole physical-chemical barrier between the steel and the exposure environment. Corrosion rate depends on ionic transport in the concrete between the anode and cathode of the electrolytic cells forming in the reinforcement [2]. Concrete physical-chemical properties therefore determine the corrosion rate. Whilst durability is an essential item in today's standards on concrete, it is not unusual in practice to find structures with poor quality cover concrete usually due to an inadequate control of the curing conditions [3].

For all this, concrete cover resistivity is an important parameter to take into account to study reinforcement durability, as it provides information about the concrete quality and its saturation degree, directly related with the corrosion process [4]. Several authors

have revealed an inversely proportional relationship between concrete resistivity and reinforcement corrosion rate [5,6]. Resistivity, along with corrosion potential, is consequently a prominent parameter in most inspection and monitoring systems [7]. Although qualitative, it is a parameter useful for detecting areas with potential risk of corrosion. Recommendations for correlating the probable corrosion risk and concrete resistivity are presented in the literature [8], where the corrosion risk of reinforcement is divided into four levels according to the magnitude of resistivity (ϱ) as exemplified at Table 1 together with corrosion risk criteria based on the corrosion rate value, expressed in terms of current density (i_{CORR}), according to references [9,10].

Table 1. Criteria for assessment of corrosion risk in terms of concrete electrical resistivity (ϱ) and corrosion current density (i_{CORR}) according to references [8–10].

Corrosion Risk	Resistivity ($\Omega \cdot cm$)	i_{CORR} ($\mu A/cm^2$)
Negligible	>100,000	<0.1
Low	50,000–100,000	0.1–0.5
Moderate	10,000–50,000	0.5–1
High	<10,000	>1

The Wenner (four electrodes) and the disc (one external electrode) methods are the benchmark techniques for in situ resistivity measurements in existing concrete structures [8]. Wickramanayake et al. [11] and Feliu et al. [12] developed outstanding sensors which operate on these respective principles. Given the utility of broaching durability problems effectively and sufficiently in advance, however, by monitoring structures from the time they are built, alternative embedded methods for monitoring resistivity have been proposed. Examples include a multi-electrode system developed by Badr et al. [13] to determine resistivity at different depths or the screen-printed sensor proposed by Sophocleous et al. [14]. Inasmuch as resistivity is particularly helpful when analyzed in conjunction with other durability parameters, the idea of integrating resistivity measurements in embedded corrosion rate assessment systems has been gaining in popularity [15,16]. In this line, Duffó et al. [17] proposed a multi-parameter sensor in which electrical resistance measured between two inert electrodes is converted to resistivity by applying a cell constant. Common commercial devices are based on this principle to determine resistivity in corrosion monitoring [18], though there are some examples that use Wenner-based sensors [19].

The need to incorporate a specific resistivity sensor into the monitoring system could involve increasing the implementation costs and complexity of the system. In addition, under certain circumstances, some resistivity sensors could reduce their reliability because the cell constants used are usually limited to very specific implementation conditions [8]. It is usually due to the use of a limited number of calibration solutions [13], as well as due to variations in the geometric features of the sensor during its implementation which have not been considered in the cell constant calibration [10]. Therefore, it is usually suggested to calibrate the cell constant in every sensor implementation to ensure reliability [10,20].

Technological advances in recent decades have also influenced the development of corrosion sensors. Among the most important proposals are fiber optic sensors [21,22], which stand out for their versatility and miniaturization capability; and sensors based on inductively coupled magnetic fields [23,24], which allow wireless monitoring. In addition, emerging damage identification techniques based on acoustic emission [25] and guided ultrasonic waves [26] have proved effective in damage identification in reinforced concrete. Despite their unquestionable advantages, at the moment these advanced methods do not provide high accuracy in corrosion rate measurements and, something which take special importance in the context of this paper, do not include the possibility of determining the electrical resistivity of concrete.

The present authors have been studying the durability issues arising around reinforced concrete for many years, focusing particularly on modelling and developing methods for corrosion rate determination [27–29]. The outcome is an innovative system of embedded sensors for monitoring corrosion in reinforced concrete structures [30,31], which we have termed INESSCOM (an acronym for Integrated Network of Sensors for Smart Corrosion Monitoring). This autonomous system can monitor several areas of a structure simultaneously and in real time using an embedded sensor in which an innovative approach with potential step voltammetry (PSV) provides a number of parameters, including corrosion rate and electrical resistance of concrete [29], but not electrical resistivity, which could limit its applicability.

Although the authors have discussed and put forward alternatives for measuring resistivity in earlier articles, those studies were geared towards the resistivity determination in laboratory studies [32]. Whilst the conclusions of those prior efforts are useful, the present study is geared toward a different perspective, namely on-site concrete resistivity determination.

The primary aim of this work was to define a reliable expression to determine resistivity from the concrete electrical resistance (R_E) provided by the INESSCOM corrosion sensor. The novelty here is that distinct from common embedded sensors, the constant cells of the proposed expression are applicable for any sensor implementation scenario. This was ensured by studying most significant geometrical features of the sensor, i.e., electrode areas, spacing and positions/setups, by using a wide set of calibration solutions which quite cover the range of values that would be expected in on-site resistivity monitoring.

This proposal was designed to be to be applicable for R_E measurements obtained both using the PSV method, implemented in the INESSCOM sensor for corrosion rate measurement, and alternating current methods. In this regard, as an added novelty, we present a simple PSV protocol to reliably determine R_E, and therefore resistivity, by using the INESSCOM corrosion sensor. This renders feasible to quick and easy monitor resistivity along with corrosion rate through a single sensor, thus eliminating the need for additional sensors, time-consuming methods or complex electronic devices; an unusual advantage in structural health monitoring.

2. Materials and Methods

2.1. Measurement Principle Governing INESSCOM Sensor

Figure 1a depicts the corrosion measurement principle governing the INESSCOM sensor we have developed and whose possible use to determine concrete resistivity is explored hereunder. The system uses potential step voltammetry (PSV) to measure corrosion rate, as described elsewhere [29]. The technique is based on the intersection method, with the added advantage that as the Tafel slopes can be found in less time, the technique is less invasive than the original method. The circuit in Figure 1b proposed in earlier studies [27] is used to model the transient response of the steel-concrete system when the potential pulse sequence shown in Figure 1c was applied. In addition to corrosion rate, the model can be used to find parameters such as the electrical resistance of concrete ($R_{E\text{-}PSV}$), based on circuit resistances R_1 and R_2 from Equation (1):

$$R_{E-PSV} = \frac{R_1 \cdot R_2}{R_1 + R_2} \tag{1}$$

The sensor needs only two elements (Figure 1a) for conducting the PSV measurement, the working (WE) and counter (CE) electrodes. The advantage of such a two-electrode setup is that, unlike standard sensors, it does not require an embedded reference electrode (RE) whose uncertain long-term stability could affect sensor reliability. The sensor may, however, optionally bear a built-in RE to measure the corrosion potential (E_{CORR}) which, although a qualitative parameter, provides more complete analyses of reinforcement condition.
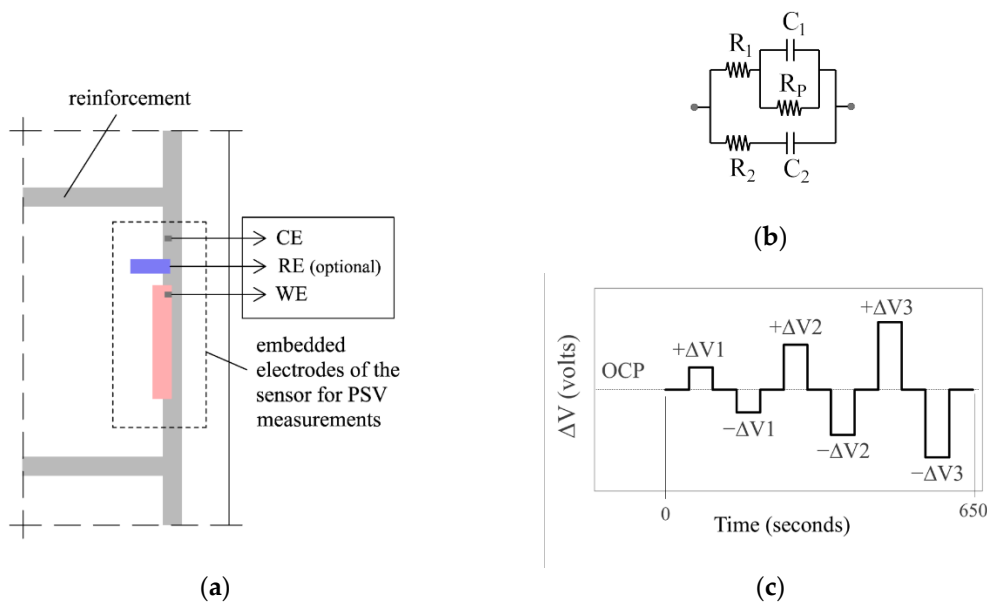
Figure 1. Embedded corrosion sensor for measuring the corrosion rate: (**a**) measuring cell used to apply PSV with the optional inclusion of a reference electrode (RE) to measure the E_{CORR}; (**b**) equivalent circuit used in PSV to model the transient response of the steel-concrete system; and (**c**) potential pulse sequence applied in PSV to polarize the system.

In the two-electrode PSV measurements (Figure 1a), the WE was a corrugated carbon steel bar with the same characteristics as the reinforcement of the structure to be monitored, but shorter and with the two ends sealed with epoxy resin to clearly delimit the working area. The CE, in turn, was the reinforcement itself of the structure to be monitored. The CE area was consequently much larger than the WE area, an arrangement shown in earlier studies [31] to be imperative for reliable two-electrode PSV measurement.

2.2. Measuring Cell

Cells were designed to measure electrical resistance (R_E) between one or several working electrodes (WE) and the counter electrode (CE) housed in the corrosion sensor described in Section 2.1. Two types of cell were used (Figures 2 and 3) to assess the maximum number of possible geometrical factors that may be relevant to R_E conversion to resistivity (ϱ).

The cell in Figure 2 was intended to assess how the CE area/WE area (S_{CE}/S_{WE}) ratio affected the sensor. Both the WE and the CE comprised several rebars that could be connected or disconnected as needed, thereby generating a wide spectrum of S_{CE}/S_{WE} ratios. In the CE, six rebars were positioned in a polymeric holder in three two-column rows and evenly spaced at 1.5 cm. The three WE (WE1, WE2 and WE3) were arranged as a single linear rebar using polymeric tubes and it was mounted on polymeric guide rails to be placed parallel at variable distances to the CE. With that setup, the cell could be used to assess the effect of the WE-CE spacing on measurements, for which purpose eight WE-CE distances were studied: 3, 8, 15, 24, 36, 45, 52 and 57 cm. This wide range of distances is intended to provide sufficient variation of the WE-CE spacing and, thus, to reliably calibrate the cell constant according this important geometrical factor of the sensor. Moreover, these WE-CE distances are in the range of usual spacing of rebars in concrete structures [33], so they can be considered realistic.
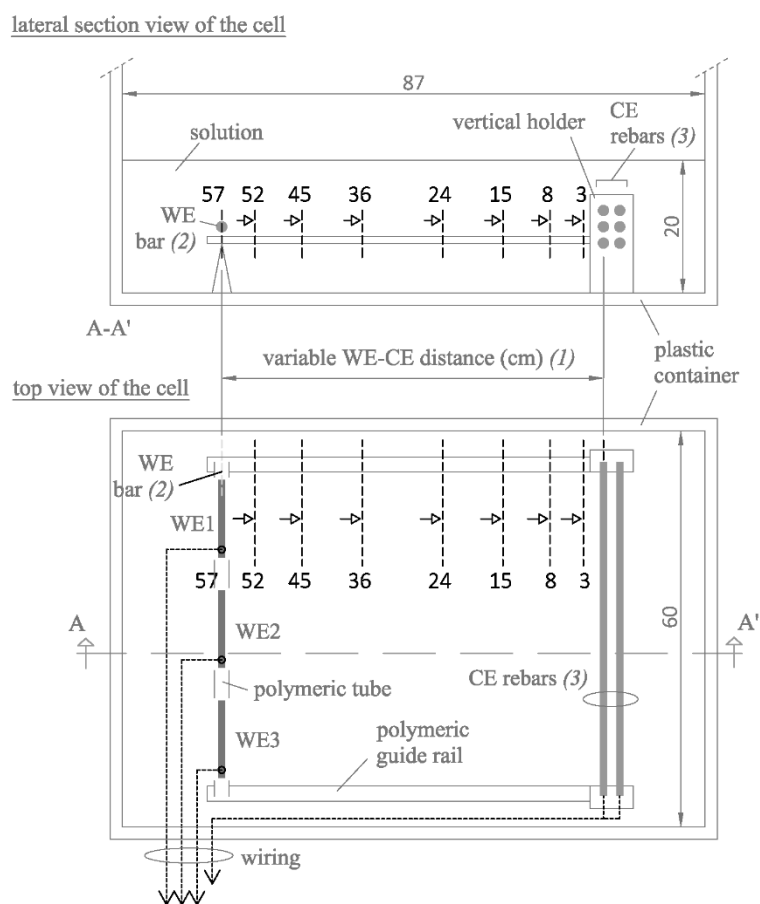
lateral section view of the cell

Figure 2. Measuring cell used to assess the effect of the S_{CE}/S_{WE} ratio and WE-CE spacing (dimensions in cm).

The cell in Figure 3 consisted in a four-rebar lattice CE, whose rebars could be connected or disconnected at will to establish different CE setups, and a single-rebar WE positioned on a rotating holder to adjust its relative position to the CE.

On the one hand, the cell in Figure 3 led to the four cell arrangements shown in Figure 4, which were used to study the effect in the case that one of the CE rebars (CE-2) is placed at a different WE-CE distance (d_2) with respect to a second CE rebar (CE-1) at a constant distance (d_1) from the WE. To do this, one of the CE rebars was mounted on lateral guide rails to be slid in 5 cm steps to progressively increase its WE-CE distance (d_2).

On the other hand, the cell in Figure 3 led to the seven WE-CE setups shown in Figure 5a, which were used to analyze how the WE position with respect the CE (arranged in various manners) affected measurements. Each setup was considered to have two possible WE orientations relative to the CE as shown in Figure 5b: (I) in parallel/perpendicular or (II) in diagonal (45°). Here, all four CE rebars were at a constant 5 cm from the WE.

All the WEs employed consisted of a corrugated carbon steel bar of 8 mm in diameter and 70 mm in length sealed at both ends by pouring epoxy resin into a polymeric tube to delimit the working area and protect the electrical connection to the copper wire installed at one of the ends. The effective working area for each WE element was 17.5 cm². The CE was made of the same steel as the WEs. Each CE rebar consisted in a rebar of 8 mm in diameter and 420 mm in length wired and sealed in the same way as the WEs. The working area of each CE rebar was 105.6 cm².

lateral section view of the cell
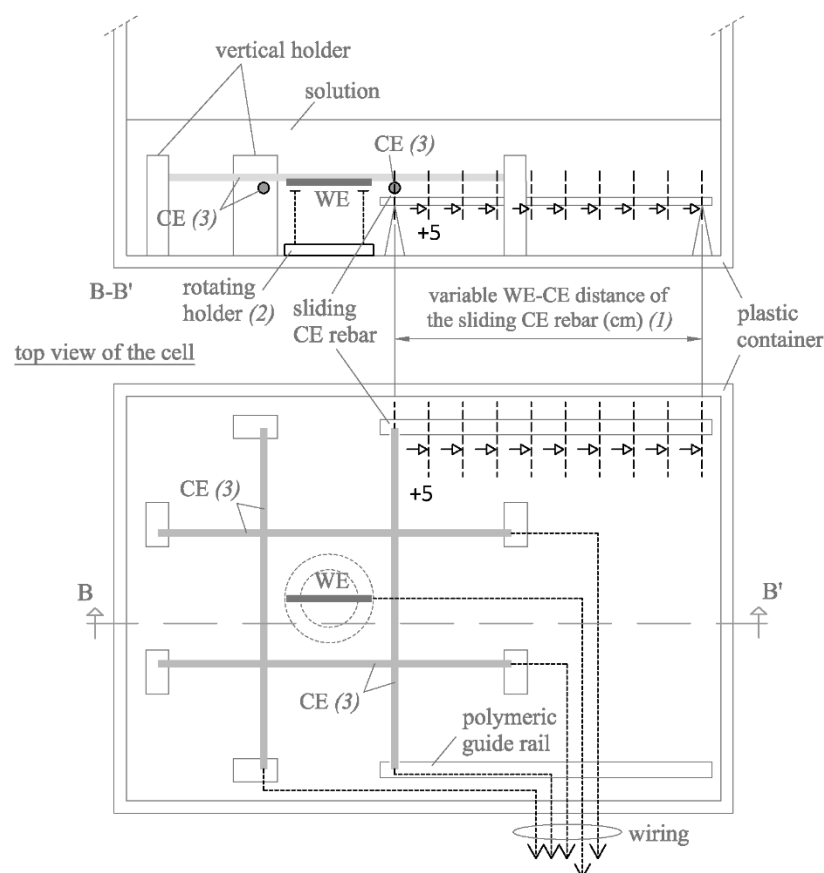
(1) achieved by moving the CE sliding rebar away from, or closer to, the WE in +5cm increments.

(2) used to position the WE in parallel/perpedicular or diagonal (45°) with respect the CE.

(3) the four CE rebars can be connected or disconnected to achieve different CE setups.

Figure 3. Measuring cell used to assess the effect of WE position relative to the rebars in the CE and the effect in the case that one of the CE rebars is placed at a different WE-CE distance with respect to all the others (dimensions in cm).
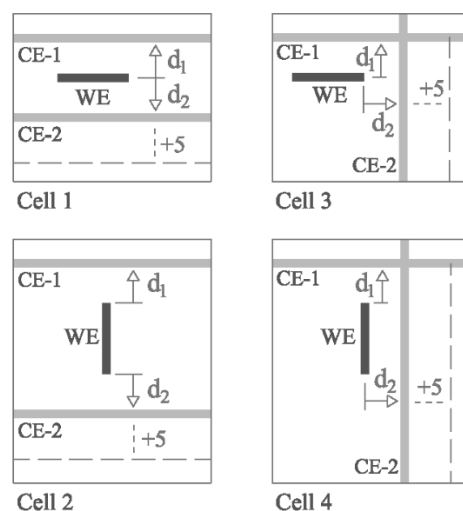

Figure 4. Four cell arrangements (from the cell in Figure 3) used to study the effect of unequal distances between the CE bars and the WE. The CE consisted in two rebars, CE-1, placed at a constant 5 cm (d_1) from the WE and CE-2, positioned at variable distances (d_2) with upward ramping at 5 cm intervals.
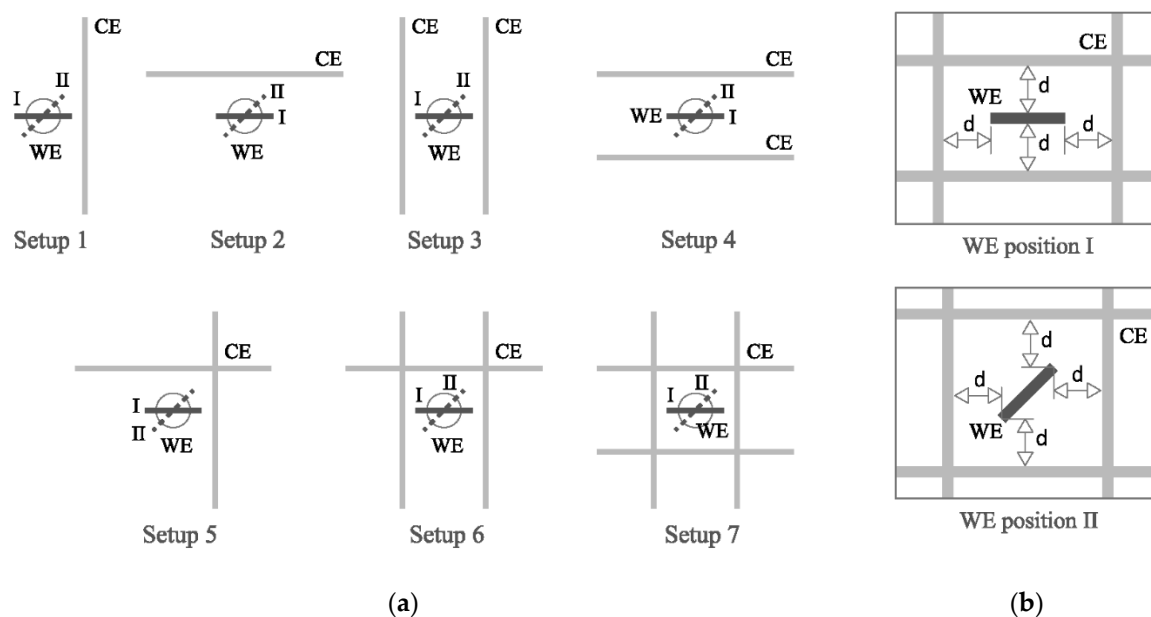
Figure 5. (**a**) Seven WE-CE setups (from the cell in Figure 3) used to assess the effect of the position of WE relative to CE on resistivity measurements; (**b**) WE positions relative to CE in the WE-CE setups: (I) parallel/perpendicular or (II) diagonal (45°).

2.3. Solutions

Measurements were taken in 15 aqueous solutions ranging in resistivity from 6.5 to 65,500 Ω·cm. This wide range of values is intended to cover as many different implementations scenarios as possible in the sensor characterization. The main field of application of the sensor is for concrete monitoring. In the case of ordinary concretes, resistivity may vary, according to [8], from 10,000 to 100,000 Ω·cm. However, less resistive concretes are also of interest, such as steel fiber [34] and carbon fiber [35] reinforced concrete.

The composition, pH and resistivity of the solutions used are listed in Table 2. Three types of solvent were used, A, B and C. Five solutions were prepared with solvent A, a saturated $Ca(OH)_2$-tap water solution (with 0.0005 mol·L^{-1} of chlorides) to simulate the solution in concrete pores. Seven solutions were based on solvent B, tap water alone in which the absence of $Ca(OH)_2$ determined higher resistivity, closer to the values characteristic of concrete. Inasmuch as solvent C consisted in deionized rather than tap water, the three resulting solutions exhibited the highest resistivity used in this study. NaCl was added at different concentrations in each set of solutions (Table 2) to vary resistivity across a broader range of values. Solution A5 (saturated $Ca(OH)_2$ with 1 mol·L^{-1} chloride) simulated concrete carbonation by adding $NaHCO_3$, which lowered the pH to 8.8. All the solutions were prepared with analytical grade reagents.

The study was performed from lower to higher chloride concentration, adding the respective amount of NaCl at each step, thereby avoiding the need to prepare a new solution for each chloride concentration in the set. Otherwise, the experiment would have been resource-intensive, for measurements were made in an 870 × 600 × 510 mm³ plastic container filled to a height of 200 mm, yielding a volume of 104.4 L of solution (Figures 2 and 3).

Table 2. Composition, chloride concentration, pH and resistivity (ϱ) of the solutions tested.

Solution ID	Solvent	Cl⁻ (mol·L⁻¹)	pH	ϱ_{COND} (Ω·cm)
A1	Ca(OH)$_2$-saturated tap water	0.0 [1]	12.54	87.10
A2	Ca(OH)$_2$-saturated tap water	0.1 [1]	12.46	38.71
A3	Ca(OH)$_2$-saturated tap water	0.5 [1]	12.23	11.92
A4	Ca(OH)$_2$-saturated tap water	1.0 [1]	11.98	6.52
A5	Ca(OH)$_2$-saturated tap water + 0.22 M NaHCO$_3$	1.0 [1]	8.88	6.60
B1	Tap water	0.0 [1]	7.50	3347.84
B2	Tap water	0.0015 [1]	8.37	1830.02
B3	Tap water	0.0032 [1]	8.54	952.40
B4	Tap water	0.014 [1]	8.71	326.80
B5	Tap water	0.021 [1]	8.03	145.77
B6	Tap water	0.1 [1]	7.80	76.16
B7	Tap water	0.5 [1]	8.76	15.38
C1	Deionised water	0.0	5.46	65,444.40
C2	Deionised water	0.0	6.62	31,237.83 [2]
C3	Deionised water	0.00037	6.56	7972.69

[1] Molar concentration of chloride without considering the contribution of the tap water used in the solvent, which is 0.0005 mol·L⁻¹. [2] After soaking in the solution for 24 h, resistivity declined due to a sensor corrosion-induced rise in Fe^{2+} and Fe^{3+} concentration.

2.4. Measuring Procedure

The WE and CE were degreased with acetone, washed in alcohol and hot-air dried prior to measuring. No surface treatment was applied after soaking to reproduce the conditions actually prevailing in the use of the sensor system in concrete. All experiments were conducted at laboratory temperature (20 ± 2 °C). The WE and CE were exposed to each volume-verified solution (Table 2) for 12 h, deemed sufficient to attain a stationary potential. Solution resistivity and temperature were subsequently measured on a Hanna Instruments HI 2300 auto-ranging resistivity meter, after which sensor measurements were undertaken.

The first parameter measured was electrical resistance (R$_E$) between the WE and CE in all the cell types and combinations in Figures 2 and 3, as described in Section 2.2, using a U1733C handheld alternating current (a.c.) LCR meter (Keysight Technologies, Santa Rosa,CA, USA). This R$_E$ measurement was contrasted with the R$_E$ value obtained by PSV technique as described in Section 2.1 for all the WE-CE distances depicted in Figure 2. The corrosion current density (i$_{CORR}$) was also obtained from the PSV measurement as described elsewhere [29]. The potential step sequence applied in the PSV measurements was as shown in Figure 1c, with ±ΔV1 = 105 mV, ±ΔV2 = 140 mV and ±ΔV3 = 175 mV relative to the open circuit potential (OCP). The R$_E$ value found was compared to the resistance determined with a 50 mV, 5 ms pulse. That fast pulse was applied to obtain a more reliable sensor response at the outset of the test (t → 0) when the non-Faraday processes that determine R$_E$ prevail. The PSV measurements were taken on a PGSTAT 100 potentiostat (Metrohm Autolab, Utrecht, The Netherlands). The OCP used was deemed in all cases to be the potential recorded between the WE and CE when the ∂E/∂t value dropped to below 0.03 mV/s.

3. Results

This study explored a simple procedure for determining resistivity (ϱ) with the INESSCOM embedded sensor described in Section 2.1. It is designed to measure corrosion rate in a two-electrode (WE and CE) setup. Equation (2), used in the two-point or direct method where the resistivity measurement is also taken between two electrodes, was consequently adopted as the initial reference:

$$\rho = R_E \cdot \frac{S}{d} \tag{2}$$

Equation (2) determines resistivity (ρ) in a concrete sample with length d and cross-section S from the electrical resistance (R_E) measured between two equal flat electrodes, likewise with cross-section S and positioned in parallel on opposite sides of the sample.

The two electrodes in the corrosion sensor used here, however, were not flat, had different cross-sections and could not be positioned in parallel. In addition, the sensor measurement is based on the Potential Step Voltammetry (PSV), whereas common methods for resistivity measurement are based on alternating current methods.

Based on these factors, and to facilitate the analysis and discussion of the results, this section has been divided into two main phases:

1) Study of the geometrical cell parameters in sensor

Here we study the different geometrical factors involved in the sensor measuring cell which could affect resistivity determination. Each factor has been varied enough to determine the most appropriate manner to be incorporated into Equation (2), i.e., as a cell constant, in order to obtain a reliable expression to determine resistivity. In consequence, this phase has been divided in different sub-sections, each one focused on a specific feature of the sensor:

(i) Electrode areas,

(ii) Electrode spacing and

(iii) Electrode arrangement.

2) Reliability of the PSV-measured R_E

Here we analyze if the R_E obtained by the PSV method (used in the sensor for corrosion rate measurement) can be directly introduced in the expression determined in the previous stage to determine resistivity or whether a feasible PSV modification is required to ensure accuracy.

3.1. Study of the Geometrical Cell Parameters in Sensor

3.1.1. Electrode Areas

Electrical resistance (R_E) was measured with the cell in Figure 2, varying the number of bars connected to the CE and to the WE. That procedure yielded measurements for nine CE area/WE area (S_{CE}/S_{WE}) ratios for each of the eight possible distances between the WE and CE. The findings for the Ca(OH)$_2$-saturated solution with 0 mol·L^{-1} of chlorides (solution A1 in Table 2) plotted in Figure 6a show that R_E values tended to stabilize at sufficiently large S_{CE}/S_{WE} ratios. Figure 6b graphs the relationship between R_E for each S_{CE}/S_{WE} ratio (termed as $R_E[i\text{-}S_{CE}/S_{WE}]$) and the R_E for the maximum S_{CE}/S_{WE} ratio (termed as $R_E[max\text{-}S_{CE}/S_{WE}]$). The difference in the measurements was <5% when CE was 12 times greater than WE, as was the case at all the distances studied.

The S_{CE}/S_{WE} threshold of >12 would be guaranteed if sensors are used to monitor reinforced concrete structures, for in such cases, as noted in Section 2.1, the CE is the reinforcement itself. It would nonetheless be useful to be able to apply resistivity for any possible S_{CE}/S_{WE} ratio. It is not unusual in research, for instance, to monitor small or lightly reinforced concrete specimens, where the sensor's S_{CE}/S_{WE} ratio is lower.

A method for normalizing R_E for any S_{CE}/S_{WE} ratio was consequently needed. In Equation (2) the R_E value is multiplied by the sensor's working area (S). The resulting coefficient of variation (C.V.) for each WE-CE distance is shown in Figure 6c. The findings showed that the C.V. for $R_E S_{WE}$ was over 15% at WE-CE distances of 3 cm to 45 cm and from 10% to 15% at distances of 52 cm to 57 cm. The C.V. declined to under 10% for $R_E S_{EQ}$, however. The parameter S_{EQ}, proposed to express the sensor's equivalent working area, is defined in terms of S_{CE} and S_{WE} as follows:
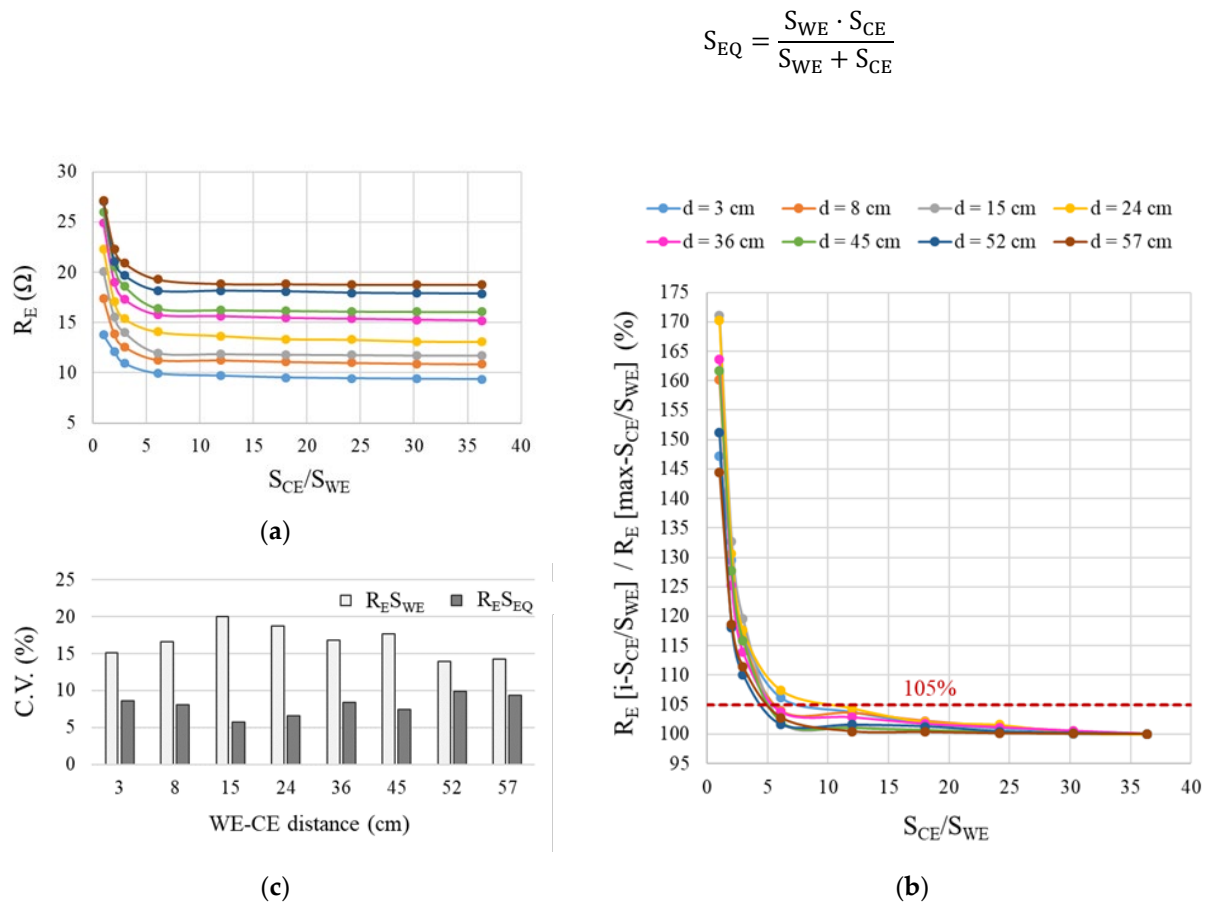
$$S_{EQ} = \frac{S_{WE} \cdot S_{CE}}{S_{WE} + S_{CE}} \quad (3)$$

Figure 6. Electrical resistance (R_E) at different WE-CE distances in a saturated Ca(OH)$_2$ solution with 0 mol·L^{-1} chlorides: (**a**) R_E vs. the S_{CE}/S_{WE} ratio; (**b**) $R_E[\text{i-}S_{CE}/S_{WE}]/R_E[\text{max-}S_{CE}/S_{WE}]$ vs. S_{CE}/S_{WE} where $R_E[\text{i-}S_{CE}/S_{WE}]$ is the R_E measured at the respective i-S_{CE}/S_{WE} and $R_E[\text{max-}S_{CE}/S_{WE}]$ is the R_E obtained for the maximum S_{CE}/S_{WE}; and (**c**) coefficient of variation in $R_E \cdot S$ depending on whether S is defined as S_{WE} or S_{EQ}.

Another factor that must be taken into consideration in Equation (3) is that the rebars comprising the CE may not all be at the same distance from the WE. Therefore, R_E was measured between the WE and a CE consisting of two bars (CE-1 and CE-2), one at a constant 5 cm (d_1) from the WE and the other at d_2, which varied. That yielded a number of d_2/d_1 ratios for all four cell arrangements depicted in Figure 4.

As Figure 7a shows, here S_{EQ} as defined in Equation (3) would not be suitable, since the $R_E S_{EQ}$ value varied upward with rising d_2/d_1 ratios in all four setups. To correct for that effect, the areas of CE-1 and CE-2 had to be used in S_{EQ} calculations in proportion to their respective distance from the WE. The proposal consequently consisted in replacing the term S_{CE} in Equation (3) with S_{CE_EQ}, as follows:

$$S_{EQ} = \frac{S_{WE} \cdot S_{CE\_EQ}}{S_{WE} + S_{CE\_EQ}} \quad (4)$$

S_{CE_EQ} is found as the sum of the equivalent areas of all the rebars comprising the CE:

$$S_{CE\_EQ} = \sum_{i=1}^{n} S_{CE-i\_EQ} \quad (5)$$

The equivalent area of each rebar (S_{CE-i_EQ}) relative to its distance from the WE (d_i) is determined from Equation (6) proposed here:

$$S_{CE-i\_EQ} = S_{CE-i} \cdot \frac{d_{MIN}}{d_i} \quad (6)$$

where d_{MIN} is the shortest distance between any of the rebars in the CE and the WE.
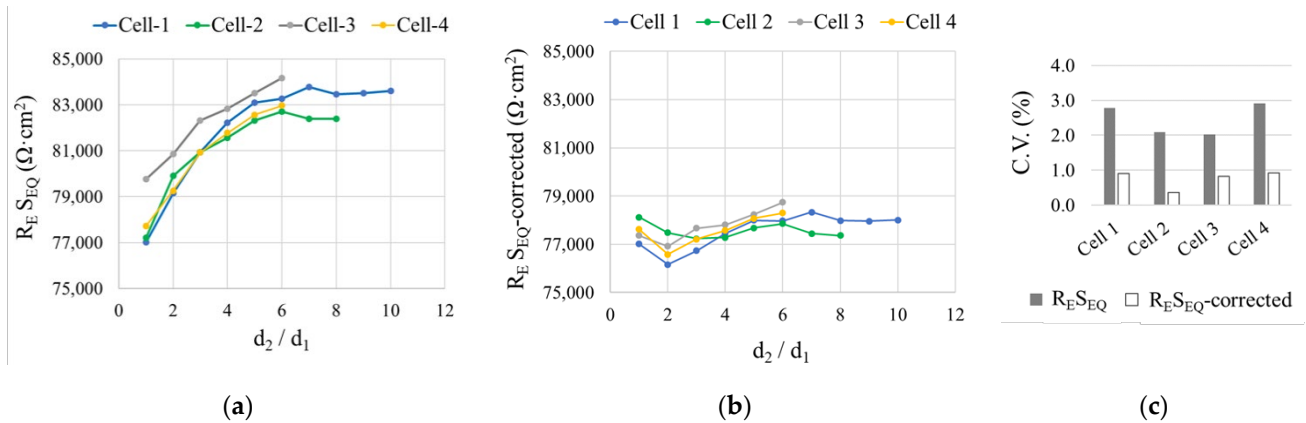

(**a**) (**b**) (**c**)

Figure 7. (**a**) R_ES_{EQ} vs d_2/d_1 for a two-rebar CE (CE-1 and CE-2), one at a fixed (d_1) and the other at a variable (d_2) WE-CE distance, using the four cells in Figure 4 in a deionized water solution with 0 mol·L⁻¹ of chlorides. (**b**) R_ES_{EQ}-corrected vs d_2/d_1. S_{EQ}-corrected results by using S_{CE_EQ} (Equation (5)) to calculate S_{EQ} (Equation (4)). (**c**) Coefficient of variation (C.V.) for R_ES_{EQ} and R_ES_{EQ}-corrected at all the d_2/d_1 ratios.

Figure 8a plots the equivalent areas of CE-1 (S_{CE-1_EQ}) and CE-2 (S_{CE-2_EQ}) as found with Equation (6) and of the respective CE (S_{CE_EQ}) calculated with Equation (5) for the d_2/d_1 ratios studied in Cell 1 as depicted in Figure 4. As CE-1 was at the shortest distance from the WE in all cases, so $d_{MIN} = d_1$ and consequently $S_{CE-1\_EQ} = S_{CE-1}$ for all d_2/d_1 ratios. Given that the distance to CE-2 from WE (d_2) varied, S_{CE-2_EQ} also varied, downward as d_2 rose. In consequence, the equivalent area of the entire CE (S_{CE_EQ}) also drops as the CE-2 distance from WE (d_2) increases (Figure 8a). When $d_2/d_1 \geq 6$, S_{CE-2_EQ} affected the value of S_{CE_EQ} by less than 5%, and, therefore (Figure 8b), it could be considered $S_{CE\_EQ} \approx S_{CE-1\_EQ}$.
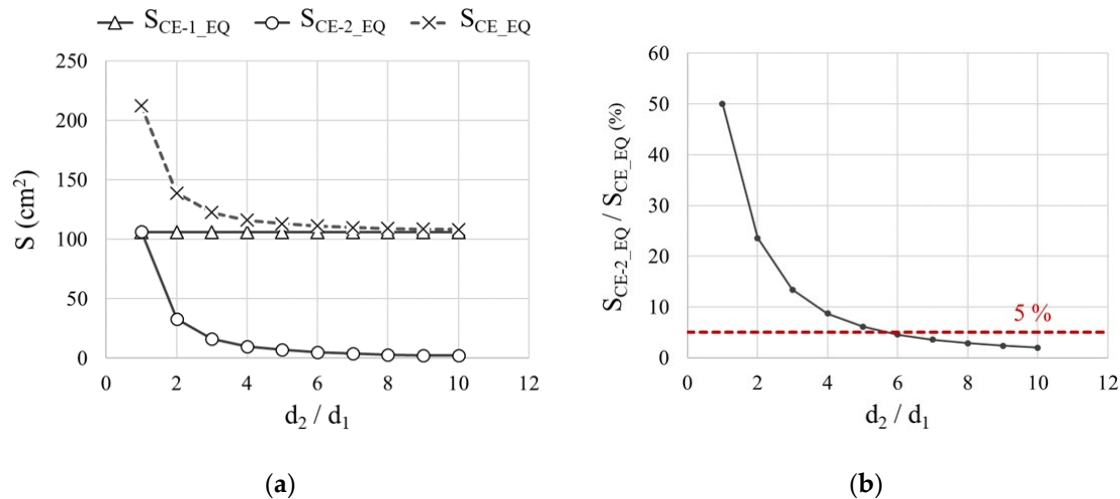

(**a**) (**b**)

Figure 8. For a two-rebar CE (CE-1 and CE-2) used in Cell 1 (Figure 4) with a deionized water solution with 0 mol·L⁻¹ of chlorides: (**a**) CE-1 and CE-2 equivalent areas (S_{CE-1_EQ} and S_{CE-2_EQ}) (Equation (6)) together with the equivalent area of the entire CE (S_{CE_EQ}) (Equation (5)) for the d_2/d_1 ratios studied. (**b**) S_{CE-2_EQ}/S_{CE-EQ} vs. d_2/d_1.

By using S_{CE_EQ} to calculate the equivalent area of the sensor (S_{EQ}) (Equation (4)), R_ES_{EQ} (referred as R_ES_{EQ}-corrected) exhibited more uniform values for all the d_2/d_1 ratios in the various cells studied (Figure 7b). That greater uniformity was mirrored in the coefficient of variation (C.V.) values shown in Figure 7c, consistently under less than 1%, i.e., smaller than the 2% to 3% calculated with Equation (3), in which the d_2/d_1 ratio was not factored in. Such finely tuned results were found by introducing an empirical constant K into Equation (6) to yield Equation (7):

$$S_{CE-i\_EQ} = S_{CE-i} \cdot \left(\frac{d_{MIN}}{d_i}\right)^K \tag{7}$$

Further to the iterations conducted, the lowest C.V. values (Figure 7c) were obtained for K = 1.7. The findings analyzed through this stage justified the reliability of S_{EQ} calculated as per Equation (4) to find resistivity from the corrosion sensor measurements.

3.1.2. Electrode Spacing

The curves in Figure 6a show that, as expected, R_E varied upward with rising distance (d) between the WE and CE in the cell depicted in Figure 2. That was attested to by the value of R_ES_{EQ}, which, for two clearly divergent distances (3 cm and 52 cm), is graphed in Figure 9a against the conductivity-meter resistivity measurements (ρ_{COND}) found in the solutions studied. The R_ES_{EQ}—ρ_{COND} relationship was observed to be linear, for as Table 3 shows, R^2 was higher than 0.9900 at all distances. The slope m on the R_ES_{EQ}—ρ_{COND} regression line varied upward with rising d, inferring that:

$$R_ES_{EQ} = \rho \cdot m \tag{8}$$

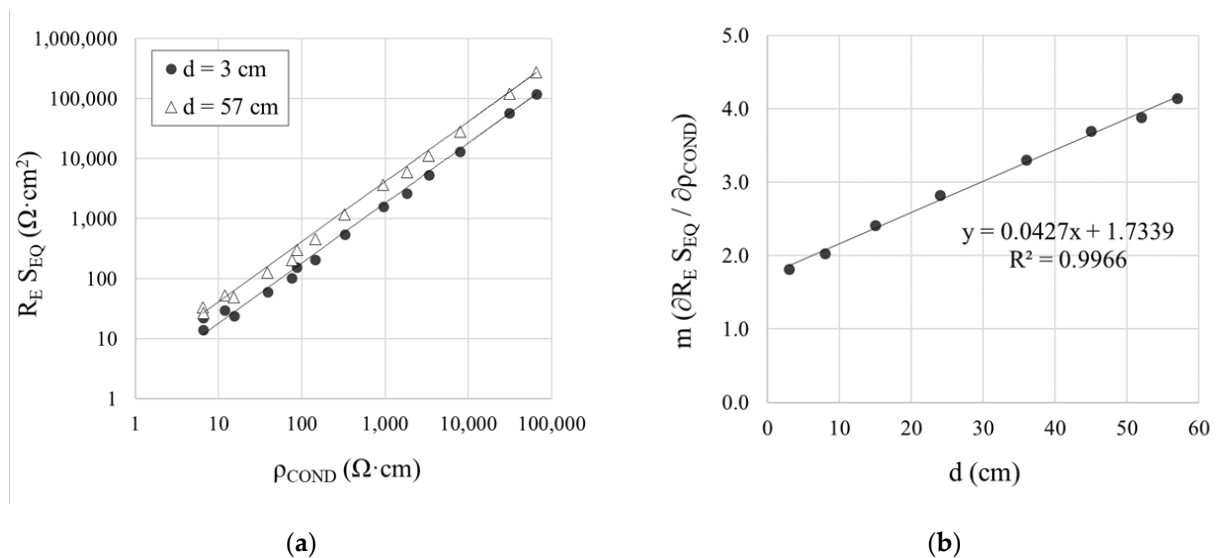(**a**)   (**b**)

Figure 9. Effect of the distance d between the WE and CE on resistivity measurements in the solutions studied: (**a**) regression line for the relationship between R_ES_{EQ} and conductivity-meter resistivity (ρ_{COND}) for the two extreme distances studied: 3 cm and 52 cm; and (**b**) regression line for the relationship between slope m ($\partial R_ES_{EQ}/\partial\rho$) and d.

Solving for ρ in Equation (8) to adopt the form of Equation (2) yielded:

$$\rho = \frac{R_ES_{EQ}}{m} \tag{9}$$

The dependence of m (regression line slope) on d (WE-CE distance) graphed in the regression line in Figure 9b is predicted by the following equation:

$$m = k1 \cdot d + k2 \tag{10}$$

where k1 and k2 are constants, respectively related to the slope and the y-intercept for regression line m-d. Substituting Equation (10) into Equation (9) yields:

$$\rho = \frac{R_ES_{EQ}}{k1 \cdot d + k2} \tag{11}$$

Equation (11) could consequently be used to obtain the resistivity for the R_E value measured between WE and CE, assuming k1 = 0.0427 and k2 = 1.7339. Given that, irrespective of how the sensor is implemented the position of WE relative to CE is known, the value of d is likewise always known.

Table 3. Slope (m) and coefficient of determination (R^2) of the linear regression between the $R_E S_{EQ}$ and the conductivity-meter resistivity (ρ_{COND}) in the solutions at the WE-CE distances (d) studied.

d (cm)	m ($\partial R_E S_{EQ}/\partial \rho_{COND}$)	R^2
3	1.6708	0.9977
8	1.8681	0.9991
15	2.2189	0.9983
24	2.5948	0.9955
36	3.0340	0.9909
45	3.3948	0.9918
52	3.5661	0.9917
57	3.8010	0.9917

3.1.3. Electrode Arrangement

As shown in Section 3.1.2, Equation (11) is useful for determining resistivity when the WE and CE are arranged in parallel in the sensor. In practice, however, other setups are possible. Such circumstances were taken into consideration with a study of the seven setups depicted in Figure 5a,b, which envisage some of the most common arrangements for installing sensors in real structures.

Table 4 gives the resistivity values determined by applying Equation (11) (ρ_{CALC}) with the measurements obtained with the various WE-CE setups. No significant differences were detected between setups or between WE positions I (parallel) and II (45°), with C.V. ≤ 2% in all the solutions studied. The graph in Figure 10 compares the ρ_{CALC} values to the conductivity-meter measurements (ρ_{COND}). The R^2 coefficient was 0.9953, which indicates a good linear correlation between both techniques. According to the slope of the regression line, sensor measurements tend to underestimate ρ by about 18% with respect to the conductivity-meter. That deviation may be deemed acceptable, given the breadth of the resistivity ranges associated with corrosion risk of steel in concrete and the absence of any single criterion on the upper and lower values in each range [6].
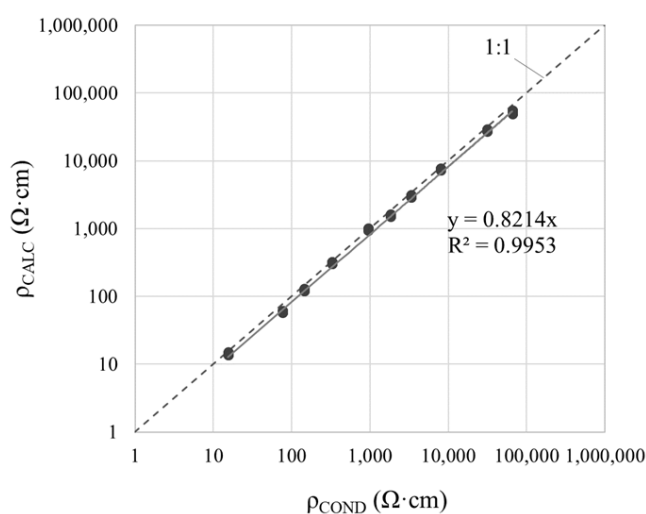

Figure 10. Linear regression between resistivity calculated (ρ_{CALC}) with Equation (11) and conductivity-meter measurements (ρ_{COND}) (ρ_{CALC} are the mean values listed in Table 4 for the WE-CE setups in Figure 5a,b using solutions B and C).

Table 4. Resistivity values found with Equation (11) (ϱ_{CALC}) using measurements in the seven setups depicted in Figure 5a,b for solutions B and C listed in Table 2, with coefficient of variation (C.V.) (%) for each and the mean ϱ_{CALC} intended to mimic the conductivity-meter resistivity measurement (ϱ_{COND}).

	Setup	WE-CE Position	Sol. B1	Sol. B2	Sol. B3	Sol. B4	Sol. B5	Sol. B6	Sol. B7	Sol. C1	Sol. C2	Sol. C3
	1	A	3065.4	1596.6	993.5	317.4	127.5	60.6	14.5	52,099.9	28,606.6	7593.8
		B	3089.1	1603.4	1001.4	321.1	128.1	61.0	14.6	54,026.0	28,607.1	7667.4
	2	A	2947.4	1546.7	963.6	309.0	123.2	58.6	14.0	50,278.2	27,738.6	7354.8
		B	2977.4	1550.8	970.8	318.8	124.2	59.1	14.0	52,281.5	27,819.7	7422.9
	3	A	3016.1	1554.3	968.0	309.4	124.8	59.2	14.3	50,967.1	27,996.0	7425.6
		B	3049.1	1602.7	999.7	320.8	128.5	61.0	14.7	55,025.0	28,714.0	7671.5
ϱ_{CALC}	4	A	2882.1	1512.9	943.7	301.3	120.9	57.5	13.7	49,424.0	27,205.1	7210.6
($\Omega \cdot$cm)		B	2990.1	1553.5	970.5	311.0	124.3	59.1	14.0	52,940.4	27,854.8	7433.1
	5	A	2978.1	1558.2	973.1	310.0	122.3	59.1	14.1	50,889.9	27,999.4	7423.9
		B	3051.6	1584.6	991.8	317.7	126.8	60.2	14.3	54,092.4	28,527.2	7580.6
	6	A	2917.1	1534.0	958.9	305.3	122.6	58.3	13.7	50,136.5	27,745.9	7330.3
		B	2990.5	1558.5	975.7	312.9	124.7	59.2	14.0	54,252.0	28,167.5	7473.7
	7	A	2937.5	1550.8	967.2	308.8	122.5	58.5	14.0	50,418.2	27,885.3	7404.2
		B	3002.5	1570.7	981.4	314.6	124.9	59.4	14.2	54,355.5	28,384.7	7525.7
		C.V. (%)	2.0	1.7	1.7	1.9	1.9	1.7	2.1	3.6	1.5	1.8
		Mean	2999.6	1562.7	975.7	312.7	124.7	59.3	14.2	52,227.6	28,089.4	7465.6
	ϱ_{COND} ($\Omega \cdot$cm)		3347.8	1830.0	952.4	326.8	145.8	76.2	15.4	65,444.4	31,237.8	8972.7

3.2. Reliability of the PSV-Measured R_E

The R_E measurements discussed in earlier sections were taken with alternating current, referred to in this section as $R_{E\text{-}AC}$. Integrating this type of measurement in the INESSCOM sensor system would entail adapting the measuring instrument to alternating current measurements, which would in turn involve more complex electronics and render the system more expensive. Hence the utility of determining R_E with the PSV technique presently built into the sensor.

As described in Section 2.1, the equivalent circuit used with the PSV technique (Figure 1b) yielded the R_E value as per Equation (1), referred to in this section as $R_{E\text{-}PSV}$. The regression lines in Figure 11a for all solutions (A, B and C) considered jointly showed a close correlation between $R_{E\text{-}PSV}$ and $R_{E\text{-}AC}$, with a downward deviation of around 11%. Although that deviation might be deemed acceptable, the values for solvent A (concrete pore solution with different chloride concentrations) were less closely aligned with the general regression trend than those for B and C. The R^2 value was in fact lower when the $R_{E\text{-}PSV}$ and $R_{E\text{-}AC}$ values were compared for set A only (Figure 8b) and deviation, upward in this case, was much greater ($\approx 400\%$).

The manner in which R_E is found in PSV ($R_{E\text{-}PSV}$) lay at the source of that deviation. Equation (1) indicates that $R_{E\text{-}PSV}$ was dependent on resistances R_1 and R_2 in the model illustrated in Figure 1b. The transient response of the model to the application of a potential step (ΔV) at $t \rightarrow 0$ depends precisely on these resistances [29]:

$$I_0 = \Delta V \cdot \left(\frac{1}{R_1} + \frac{1}{R_2} \right) = \frac{\Delta V}{R_{E-PSV}} \tag{12}$$

The $R_{E\text{-}PSV}$ value was consequently found to be inversely proportional to current intensity at $t \rightarrow 0$ (I_0):

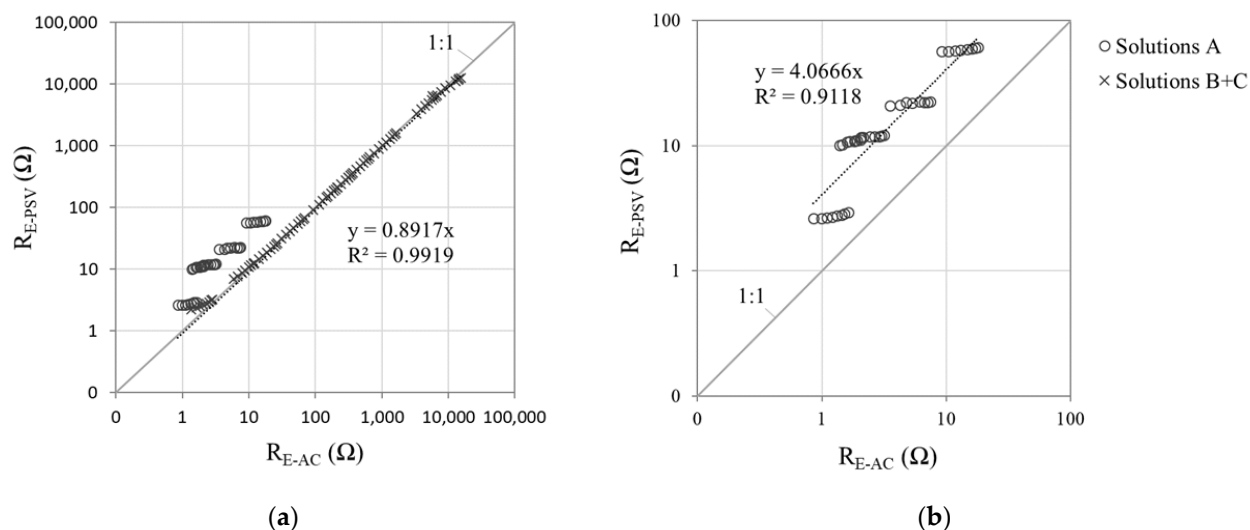$$R_{E-PSV} = \frac{\Delta V}{I_0} \tag{13}$$

Figure 11. PSV-measured electrical resistance (R_{E-PSV}) with the pulse sequence depicted in Figure 1c (sampling time, τ = 100 ms) versus the value found with alternating current (R_{E-AC}): (**a**) regression line for solutions in solvents A, B and C, taken jointly; and (**b**) regression for the five solutions bearing solvent A.

Further to Equation (13), the reliability of R_{E-PSV} depends on whether the value of I_0 can be accurately recorded with PSV measurements. The pulse sequence used in PSV (Figure 1c) was designed with a 50 s pulse duration and sampling time (τ) of 100 milliseconds. The amount of information recorded under those circumstances was moderate enough for suitable handling, although at the expense of information loss at short times (<0.1 s). That effect was attributed to the deviations in R_E observed in Figure 11 for solutions A.

Figure 12 compares the sensor's PSV current-time (I-t) response observed for solution A1 to the response for solution B4, both with a very similar R_{E-PSV} value ($\approx$53 Ω to 60 Ω), but at some distance from the R_{E-AC} reference value (14.8 Ω) in A1. For readier comprehension, the comparison focused on the pulse at $+\Delta V1$ = 105 mV (Figure 1c), whose fitting parameters for the model in Figure 1b, along with the corrosion current density (i_{CORR}) and R_{E-PSV} values recorded during the full PSV test, are given in Table 5.
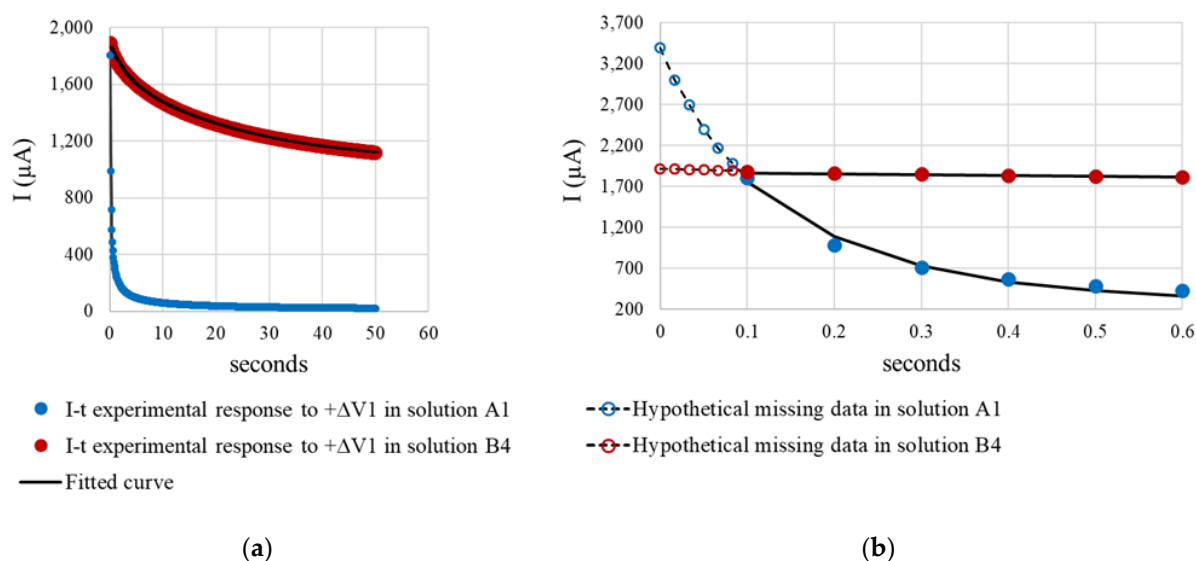

Figure 12. PSV-measured sensor current intensity—time (I-t) response in solutions A1 and B4 for the $+\Delta V1$ = 105 mV pulse of the sequence in Figure 1c: (**a**) full I-t response for the 50 s pulse and fitted curve using the model in Figure 1b, and (**b**) response from 0 to 0.6 s, showing the hypothetical part of the curve not recorded prior to 0.1 s.

The shape of the respective I-t curves (Figure 12a) and the R_P and i_{CORR} values (Table 5) denoted the existence of two very distinct electrochemical systems. As corrosion kinetics were much slower in A1 (i_{CORR} = 0.672 μA/cm^2) than in B4 (i_{CORR} = 24.763 μA/cm^2), capacitors C_1 and C_2 are related with the double layer capacitance at the steel-concrete interface (model in Figure 1b) exhibited much lower capacitance in A1 (9412.2 μF and 2225.1 μF) than in B4 (149,367.5 μF and 232,447.5 μF). That explained why current decays abruptly at early times (t < 0.6 s) in A1 while barely varying in B4 (Figure 12b). As Figure 12b shows, then, failing to record the I-t response in A1 for t < 0.1 s may entail greatly underestimating I_0, whereas in B4 the hypothetical I_0 value would barely vary. Hence the overestimation (with Equation (13)) of the R_E value in A1 (Figure 11b).

Table 5. Fitting-curve results for the $+\Delta V1$ = 105 mV pulse (Figure 1c) in solutions A1 and B4, showing the value found for the model components (Figure 1b) along with corrosion current density (i_{CORR}) and electrical resistance from the original PSV test (R_{E-PSV}), and the electrical resistance measured with alternating current (R_{E-AC}).

Solution		A1	B4
Curve fitting parameters (for $+\Delta V1$)	R_1 (Ω)	327.2	163.4
	R_2 (Ω)	72.8	86.0
	C_1 (μF)	9412.2	149,367.5
	C_2 (μF)	2225.1	232,447.5
	R_P (Ω)	3316.8	15.2
	R_E (Ω)	59.5	56.4
Final PSV results	i_{CORR} (μF/cm^2)	0.672	24.763
	R_{E-PSV} (Ω)	**59.3**	**53.6**
R_{E-AC} (Ω)		**14.8**	**54.6**

The inference of the foregoing discussion around Figure 12b is that reliable R_{E-PSV} measurement entails the use of short sampling times to suitably record I_0. Here, as an alternative to the sequence in Figure 1c, a 50 mV, 5 ms pulse was used with sampling time τ = 0.1 ms. As Figure 13a shows, the first point recorded was taken as I_0, and R_{E-PSV} was determined with Equation (11). With that approach, as the R_{E-PSV} versus R_{E-AC} regression line in Figure 13b shows, no differences in trend were detected for any of the solutions with solvents A, B or C. That procedure consequently corrected the overestimation of R_E found for the A solvent solutions using 50 s PSV pulses (Figure 11a), for the deviation between R_{E-PSV} and R_{E-AC} was consistently lower than 12%.
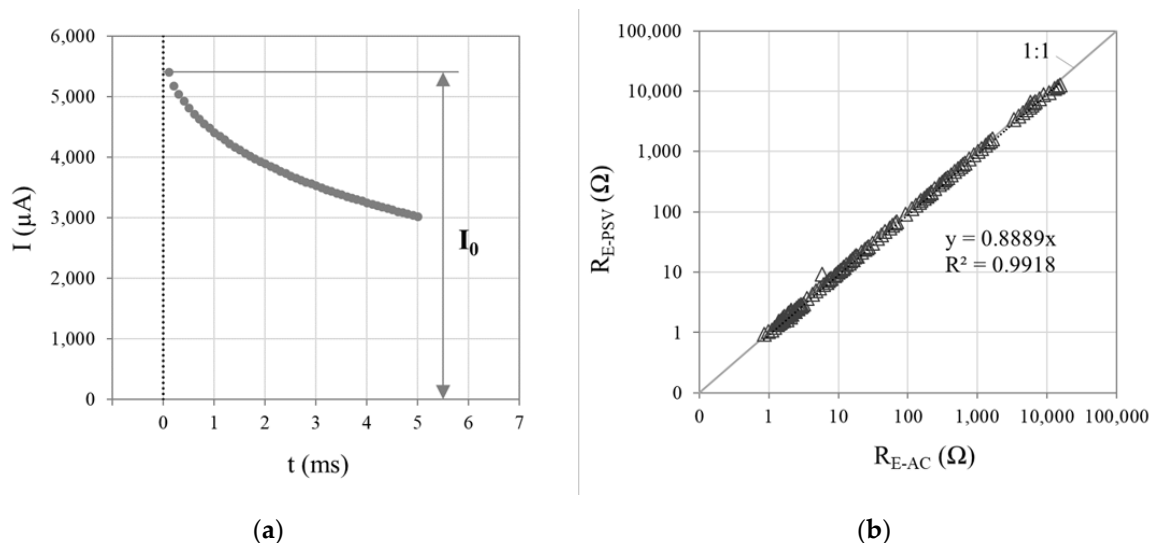

(**a**)

(**b**)

Figure 13. (**a**) Procedure used in the current-time response to a short 50 mV, 5 ms pulse (sampling time τ = 0.1 ms) to find the current at t→0 (I_0) required to determine R_{E-PSV} with Equation (13); and (**b**) R_{E-PSV} versus R_{E-AC} regression line for solutions bearing solvent A, B or C, considered jointly.

4. Discussion

The discussion in Sections 3.1–3.2 above resulted in Equation (11), an expression with reliable constant cells to determine resistivity from the R_E provided by the INESSCOM embedded sensor. This requires, as identified in Section 3.2, to include a 5 ms, $\tau = 0.1$ ms pulse prior to the original PSV technique used to determine corrosion rate (Figure 13a) Based on these findings, the respective procedure for measuring resistivity based on sensor PSV measurement is illustrated in the flow chart presented in Figure 14.
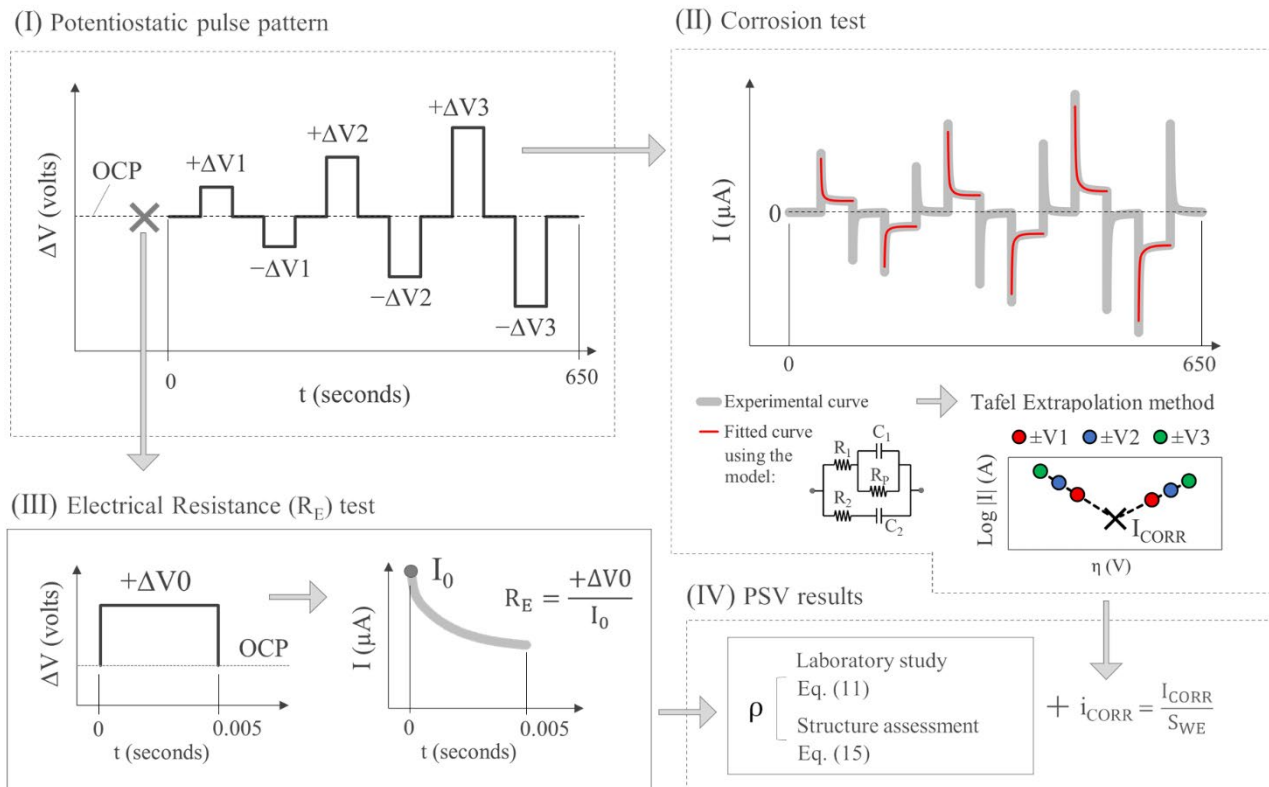
Figure 14. Procedure proposed for resistivity determination by means the PSV technique used in the corrosion sensor described in Section 2.1: (I) potentiostatic pulse sequence applied; (II) test for determining corrosion current density (i_{CORR}) by applying the Tafel extrapolation method from the modelled I-t response; (III) test proposed to be included in PSV to determine the R_E from the current at $t \to 0$ (I_0) recorded for the I-t response at a $+\Delta V0 = 50$ mV, 5 ms pulse; and (IV) final PSV results.

It should be noted, however, that Equation (11) could be simplified. Given that k1 = 0.0427 and k2 = 1.7339, the product k1·d will practically always be much smaller than k2, whereby the denominator in Equation (11) is not substantially altered by the value of d. Assuming, then, k2 >>> k1·d, Equation (11) can be simplified as follows:

$$\rho = \frac{R_E S_{EQ}}{k2} = \frac{R_E S_{EQ}}{1.7339} \tag{14}$$

In a similar vein, although S_{EQ} can be readily determined from S_{WE} and S_{CE} (Equation (4)) in scaled-down concrete specimens, the S_{CE} value is not always easy to establish in large structures. As the $S_{CE} >>> S_{WE}$ assumption holds in such cases, however, there S_{EQ} may be deemed to be approximately equal to S_{WE}. Applying that simplification to Equation (14) yields:

$$\rho = \frac{R_E S_{WE}}{1.7339} \tag{15}$$

Equation (15) is consequently a simplified expression for determining ϱ in reinforced concrete structures by using the corrosion sensor described in Section 2.1 and the procedure illustrated in Figure 14.

For a better understanding, Appendix A includes a case study of the embedded-sensor approach proposed for concrete resistivity determination. In addition to the foregoing, it should be noted that the ultimate objective of the embedded sensor approach for resistivity determination is to assess the corrosion risk of the reinforcements arising from the cover concrete properties (porosity, pore fluid chemistry, level of pore saturation, temperature, etc.). Indeed, as is known, there is an inversely proportional relationship between concrete resistivity and reinforcement corrosion rate [5,6].

This correlation is confirmed in Figure 15, which compares resistivity (ϱ) and corrosion current density (i_{CORR}), both measured using the procedure proposed in Figure 14 for the different WE-CE distances studied in the cell of Figure 2. The comparison is focused in solutions B1, B2, B3, C1, C2 and C3, since their resistivity range (Table 2) most closely align with those expected for concrete (Table 1). It is observed an excellent coincidence between the corrosion risk determined from resistivity and from i_{CORR}. Therefore, this suggest good reliability of the embedded-sensor approach proposed. However, it should be noted that, as it is known, resistivity is directly affected by temperature [36]. In consequence, temperature should be monitored along with resistivity where temperature cannot be controlled, that is, in field implementations of the INESSCOM sensor. In this way, a temperature correction factor could be determined and applied to reliably determine resistivity. Deeper discussion about this point along with validation of the proposal in concrete specimens will be reported in forthcoming papers.
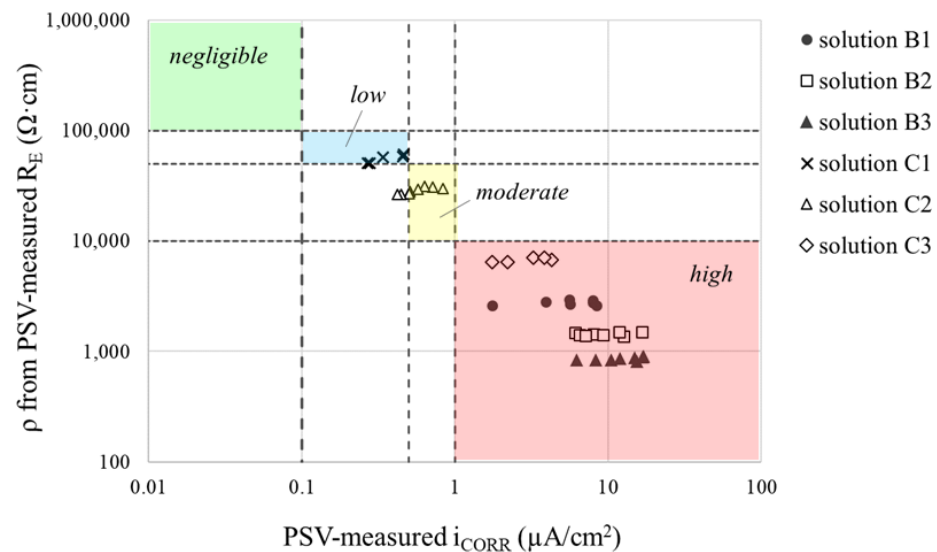

Figure 15. Comparison of resistivity (ϱ) and corrosion current density (i_{CORR}) obtained by using the procedure in Figure 14 for the different WE-CE distances studied in solutions B1, B2, B3, C1, C2 and C3. The four corrosion risk levels depicted are in accordance with Table 1.

5. Conclusions

We have proposed a reliable expression to determine concrete resistivity from the concrete electrical resistance (R_E) provided by the embedded corrosion sensor built into the Integrated Network of Sensors for Smart Corrosion Monitoring (INESSCOM) we have developed. This sensor operates using two electrodes: a carbon steel rebar as working electrode (WE) and the reinforcement itself as counter-electrode (CE). The primary goal was to find cell constants valid for any implementation scenario. The conclusions drawn from studying the most significant geometrical features of the sensor in a wide set of calibration solutions are set out below:

1) The expression $\rho = R_E \cdot S_{EQ}/(k1 \cdot d + k2)$ is proposed for determining resistivity (ρ) from the R_E measured between the WE and CE. Constants are k1 = 0.0427 and k2 = 1.7339. S_{EQ} is the sensor's equivalent area calculated from the area of WE (S_{WE}) and CE (S_{CE}) as $S_{EQ} = S_{WE} \cdot S_{CE}/(S_{WE} + S_{CE})$ and d is the WE-CE spacing. The reliability of that calculation is unaffected by how the WE and CE are arranged.

2) Where the CE comprises *n* rebars at unequal WE-CE distances, the resulting CE area (S_{CE_EQ}) is the sum of the equivalent area of each of the *n* rebars ($S_{CE\text{-}i\text{-}EQ}$). That calculation assumes $S_{CE\text{-}i\_EQ} = S_{CE\text{-}i} \cdot (d_{MIN}/d_i)^K$, i.e., $S_{CE\text{-}i\_EQ}$ is the area of the rebar itself ($S_{CE\text{-}i}$) multiplied by its WE-CE distance (d_i) divided by the minimum WE-CE distance in the CE (d_{MIN}). An experimental constant, K = 1.7, is required for maximum accuracy.

3) In electrochemical systems with low corrosion rate and low resistivity, the potential step voltammetry (PSV) technique deployed in the sensor does not provide accurate R_E measurements. Consequently, a short sampling time (1 ms) pulse must be added to the original PSV method to provide reliable R_E values with a downward deviation of <12% relative to alternating current measurements.

4) The proposal herein presented for resistivity determination is applicable for R_E measurements obtained both using the PSV method (INESSCOM) and alternating current methods. The advantage of using INESSCOM is the possibility of monitoring resistivity along with corrosion rate through a single sensor, which is not usual in structural health monitoring.

5) The corrosion risk estimations obtained from the resistivity provided by the sensor approach correlated well with corrosion current density determinations in solutions with resistivity close to ordinary concrete values. Deeper discussion about this point along with validation of the proposed resistivity expression using concrete specimens will be reported in forthcoming papers.

Appendix A

This appendix illustrates a study case on the application of the INESSCOM embedded-sensor approach proposed in this work to determine the concrete resistivity in a hypothetical reinforced concrete specimen. The scheme of the specimen and the sensor setup is evidenced in Figure A1. The corrosion-sensor electrodes, the working electrode (WE) and the counter-electrode (CE), are embedded in the specimen. The WE is a single short

rebar physically isolated from the CE. The CE is the reinforcement itself of the specimen, which consists of five rebars (A, B, C, D and E), each of which (CE-i) is initially numbered according to its distance from the WE (d_i) (from smaller to greater WE-CE distance); that is CE-1 (at d_1) = rebar C, CE-2 (at d_2) = rebar D, CE-3 (at d_3) = rebar E, CE-4 (at d_4) = rebar B, CE-5 (at d_5) = rebar A.

To determine the resistivity in the specimen depicted in Figure A1 using the embedded-sensor approach proposed, the following steps must be taken: (1) Determination of the characteristics of the sensor cell, (2) Measurement of the electrical resistance of concrete (R_E) and (3) Calculation of the concrete resistivity (ϱ). These steps are described in detail in the Sections A.1, A.2 and A.3 that follow.
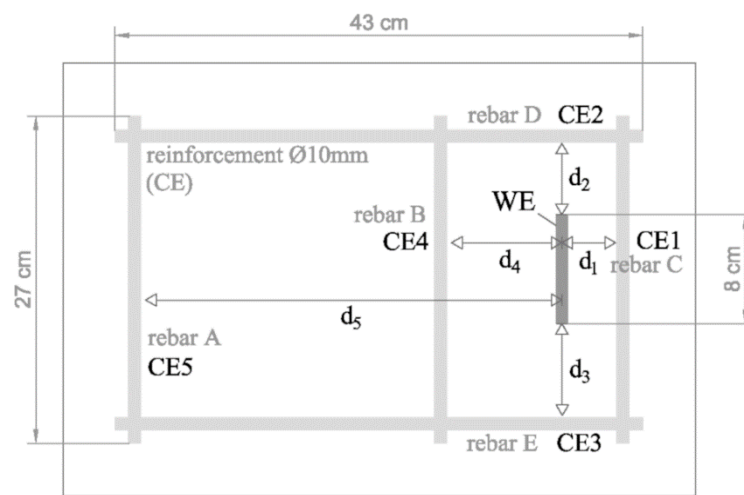

Figure A1. Scheme of the hypothetical reinforced concrete specimen considered in the study case on the application of the embedded-sensor approach proposed in this work to determine the concrete resistivity. The set-up of the corrosion-sensor electrodes (WE and CE) are depicted.

Appendix A.1. Determination of the Characteristics of the Sensor Cell

The characteristics of the sensor cell should be collected by using Tables A1–A3 prior to initiation of the measurements.

Table A1. Calculation of the Working Electrode area (S_{WE}).

Working Electrode Area (S_{WE})	$S_{WE} = 2\pi \cdot \phi/2 \cdot \text{length} = 2\pi \cdot 0.5 \text{ cm} \cdot 8 \text{ cm} = \textbf{25.1 cm}^2$

Table A2. Analysis of the characteristics of the Counter-Electrode (CE) and calculation of the Counter-Electrode equivalent area (S_{CE_EQ}).

CE ID. According to the WE-CE Distance (from Smaller to Larger)	CE-1	CE-2	CE-3	CE-4	CE-5
Rebar id.	Rebar C	Rebar D	Rebar E	Rebar B	Rebar A
WE-CEi distance (d_i)	$d_1 = 5$ cm	$d_2 = 6.5$ cm	$d_3 = 8$ cm	$d_4 = 10$ cm	$d_5 = 35$ cm
CE-i area (S_{CE-i}) *	84.8 cm²	135.1 cm²	135.1 cm²	84.8 cm²	84.8 cm²
d_i/d_{MIN}	1	1.3	1.6	2	7
Rebar to be considered? ($d_i/d_{MIN} \leq 6$)	Yes	Yes	Yes	Yes	No
CE-i equivalent area (S_{CE-i_EQ}) $S_{CE-i\_EQ} = S_{CE-i} \cdot \left(\dfrac{d_{MIN}}{d_i}\right)^{1.7}$	84.8 cm²	86.5 cm²	60.8 cm²	26.1 cm²	-
Equivalent total area of the CE (S_{CE_EQ})	$S_{CE\_EQ} = S_{CE-1\_EQ} + S_{CE-2\_EQ} + S_{CE-3\_EQ} + S_{CE-4\_EQ}$ $S_{CE\_EQ} = 84.8 + 86.5 + 60.8 + 26.1 = \textbf{258.2 cm}^2$				

$$S_{CE\_EQ} = \sum_{i=1}^{n} S_{CE-i\_EQ}$$

* Calculated in the same way as for the S_{WE} in Table A1.

Table A3. Calculation of the equivalent area of the Sensor (S_{EQ}).

S_{CE_EQ}/S_{WE} **Ratio**	$S_{CE\_EQ}/S_{WE} = 258.2/25.1 = 10.3$
If $S_{CE\_EQ}/S_{WE} \geq 12$:	No
$S_{EQ} \cong S_{WE}$	-
If $S_{CE\_EQ}/S_{WE} < 12$:	Yes
$S_{EQ} = \dfrac{S_{WE} \cdot S_{CE\_EQ}}{S_{WE} + S_{CE\_EQ}}$	$S_{EQ} = \dfrac{25.1 \cdot 258.2}{25.1 + 258.2} = \mathbf{22.9\ cm^2}$

Appendix A.2. Measurement of the Electrical Resistance (R_E) of Concrete

Appendix A.2.1. PSV-Measured R_E

Figure A2 shows an example of application of the protocol to determine the electrical resistance (R_E) of concrete by using the PSV technique integrated in the INESSCOM system. The hypothetical R_E value obtained is presented in Table A4.
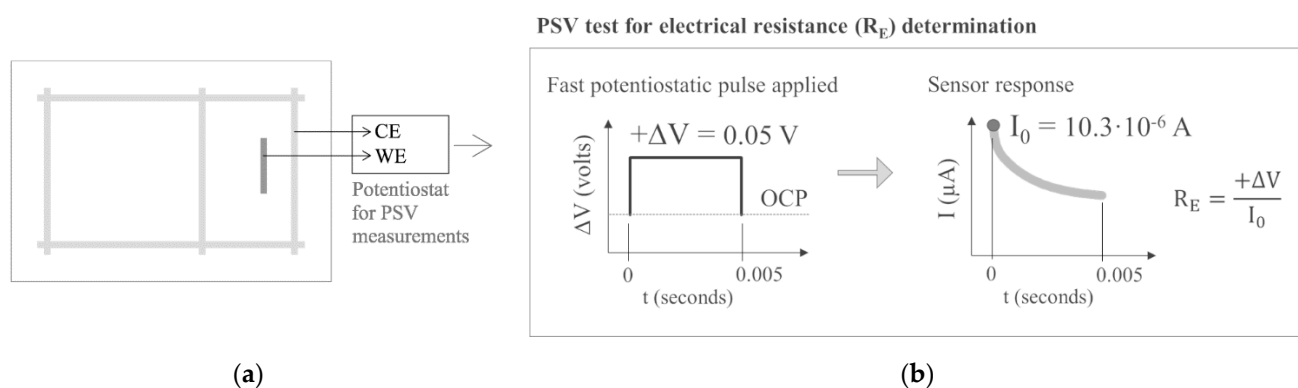

(**a**) (**b**)

Figure A2. Scheme of the protocol to determine de electrical resistance (R_E) of concrete by using the PSV technique (implemented in the INESSCOM sensor): (**a**) two-electrode set-up of the corrosion sensor which is connected to the potentiostat used in INESSCOM for PSV measurements; and (**b**) fast potentiostatic pulse (+ΔV) applied to polarize the sensor and R_E determination from the intensity response of the sensor at $t \rightarrow 0$ (I_0).

Table A4. Calculation of the electrical resistance (R_E) of concrete according to the protocol depicted in Figure A2.

$$R_E = \frac{+\Delta V}{I_0} = \frac{+0.05\ V}{10.3 \cdot 10^{-6}\ A} = \mathbf{4854.4\ \Omega}$$

Appendix A.2.2. Alternating Current Methods to Measure R_E

The R_E can be also obtained by using resistance-meter equipment based on alternating current (AC) measurements with a frequency between 50 and 1000 Hz.

Appendix A.3. Calculation of Concrete Resistivity

The resistivity of concrete (ρ) is determined from the R_E measurement with the embedded sensor by applying one of the two equations presented in Table A5.

Table A5. Calculation of the resistivity of concrete (ϱ) from the R_E measurement with the embedded sensor.

Standard Calculation

$$\rho = \frac{R_E S_{EQ}}{k1 \cdot d + k2} \qquad\qquad \rho = \frac{4854.4\ \Omega \cdot 22.9\ cm^2}{0.0427 \cdot 5\ cm + 1.7339} = \mathbf{57,080\ \Omega \cdot cm}$$

$$k1 = 0.0427$$
$$k2 = 1.7339$$
$$d = d_{MIN}$$

Simplified Calculation
(Use if $S_{CE} \ggg S_{WE}$, i.e., in Large Structures)

$$\rho = \frac{R_E S_{WE}}{1.7339} \qquad\qquad \text{---}$$

References

1. Hansson, C. An introduction to corrosion of engineering materials. In Corrosion of Steel in Concrete Structures; Elsevier Science, London: 2016; pp. 3–18, ISBN 9781782423812. https://doi.org/10.1016/B978-1-78242-381-2.00001-8.
2. Zaccardi, Y.A.V.; Di Maio, Ángel, A. Electrical resistivity measurement of unsaturated concrete samples. *Mag. Concr. Res.* **2014**, *66*, 484–491, doi:10.1680/macr.13.00207.
3. Mackechnie, J.R.; Alexander, M.G. Repair principles for corrosion-damaged reinforced concrete structures. *Res. Mono-graph.* **2001**, *5*, 27.
4. López, W.; González, J. Influence of the degree of pore saturation on the resistivity of concrete and the corrosion rate of steel reinforcement. *Cem. Concr. Res.* **1993**, *23*, 368–376, doi:10.1016/0008-8846(93)90102-f.
5. Feliu, S.; González, J.A.; Andrade, C. Relationship between conductivity of concrete and corrosion of reinforcing bars. *Br. Corros. J.* **1989**, *24*, 195–198, doi:10.1179/000705989798270027.
6. Hornbostel, K.; Larsen, C.K.; Geiker, M.R. Relationship between concrete resistivity and corrosion rate—A literature review. *Cem. Concr. Compos.* **2013**, *39*, 60–72, doi:10.1016/j.cemconcomp.2013.03.019.
7. Figueira, R.B. Electrochemical sensors for monitoring the corrosion conditions of reinforced concrete structures: A review. *Appl. Sci.* **2017**, *7*, 1157, doi:10.3390/app7111157.
8. Polder, R.B. Test methods for on site measurement of resistivity of concrete—A RILEM TC-154 technical recommendation. *Constr. Build. Mater.* **2001**, *15*, 125–131, doi:10.1016/s0950-0618(00)00061-1.
9. *UNE 112072:2011 Spanish Standard*. Laboratory Measurement of Corrosion Speed Using the Polarization Resistance Technique. 2011.
10. McCarter, W.; Vennesland, Øystein Sensor systems for use in reinforced concrete structures. *Constr. Build. Mater.* **2004**, *18*, 351–358, doi:10.1016/j.conbuildmat.2004.03.008.
11. Wickramanayake, S.; Thiyagarajan, K.; Kodagoda, S.; Piyathilaka, L. Frequency sweep based sensing technology for non-destructive electrical resistivity measurement of concrete. In Proceedings of the 36th International Symposium on Automation and Robotics in Construction, ISARC 2019, Banff Alberta, AB, Canada, 21–24 May 2019.
12. Feliu, S.; Andrade, C.; González, J.A.; Alonso, C. A new method forin-situ measurement of electrical resistivity of reinforced concrete. *Mater. Struct.* **1996**, *29*, 362–365, doi:10.1007/bf02486344.
13. Badr, J.; Fargier, Y.; Palma-Lopes, S.; Deby, F.; Balayssac, J.-P.; Delepine-Lesoille, S.; Cottineau, L.-M.; Villain, G. Design and validation of a multi-electrode embedded sensor to monitor resistivity profiles over depth in concrete. *Constr. Build. Mater.* **2019**, *223*, 310–321, doi:10.1016/j.conbuildmat.2019.06.226.
14. Sophocleous, M.; Savva, P.; Petrou, M.F.; Atkinson, J.K.; Georgiou, J. A Durable, screen-printed sensor for in situ and real-time monitoring of concrete's electrical resistivity suitable for smart buildings/cities and IoT. *IEEE Sens. Lett.* **2018**, *2*, 1–4, doi:10.1109/lsens.2018.2871517.
15. McCarter, W.J.; Chrisp, T.; Starrs, G.; Basheer, P.; Blewett, J. Field monitoring of electrical conductivity of cover-zone concrete. *Cem. Concr. Compos.* **2005**, *27*, 809–817, doi:10.1016/j.cemconcomp.2005.03.008.
16. Martínez, I.; Andrade, C. Examples of reinforcement corrosion monitoring by embedded sensors in concrete structures. *Cem. Concr. Compos.* **2009**, *31*, 545–554, doi:10.1016/j.cemconcomp.2009.05.007.
17. Duffó, G.S.; Farina, S.B. Development of an embeddable sensor to monitor the corrosion process of new and existing reinforced concrete structures. *Constr. Build. Mater.* **2009**, *23*, 2746–2751, doi:10.1016/j.conbuildmat.2009.04.001.
18. Camur II ResMes. Available online: https://www.protector.no/en/support/support/camur-ii/camur-ii-datasheets/camur-ii-technical-datasheets/resmes.html (accessed on 16 March 2021).

19. Reiss, R.A.; Gallaher, M.; California. Department of Transportation. Materials Engineering and Testing Services. Evaluation of the VTI ECI-1 Embedded Corrosion Instrument. (Report No. FHWA/CA/TL-2003/07/ECI-1). California Dept. of Transportation. 2006. Available online: https://trid.trb.org/view/794688 (accessed on 16 March 2021).

20. López-Sánchez, M.; Mansilla-Plaza, L.; Sánchez-De-Laorden, M. Geometric factor and influence of sensors in the establishment of a resistivity-moisture relation in soil samples. *J. Appl. Geophys.* **2017**, *145*, 1–11, doi:10.1016/j.jappgeo.2017.07.011.

21. Gao, J.; Wu, J.; Li, J.; Zhao, X. Monitoring of corrosion in reinforced concrete structure using Bragg grating sensing. *NDT E Int.* **2011**, *44*, 202–205, doi:10.1016/j.ndteint.2010.11.011.

22. Fan, L.; Bao, Y.; Meng, W.; Chen, G. In-situ monitoring of corrosion-induced expansion and mass loss of steel bar in steel fiber reinforced concrete using a distributed fiber optic sensor. *Compos. Part B Eng.* **2019**, *165*, 679–689, doi:10.1016/j.compositesb.2019.02.051.

23. Andringa, M.M.; Neikirk, D.P.; Dickerson, N.P.; Wood, S.L. Unpowered wireless corrosion sensor for steel reinforced con-crete. *Proc. IEEE Sensors* **2005**, *2005*, 155–158.

24. Andringa, M.M.; Puryear, J.M.; Neikirk, D.P.; Wood, S.L. In situ measurement of conductivity and temperature during concrete curing using passive wireless sensors. *Proc. 14th Int. Symp. Smart Struct. Mater. Nondestruct. Eval. Health Monit. SPIE-Int. Soc. Opt. Eng.* **2007**, *6529*, 65293M.

25. Degala, S.; Rizzo, P.; Ramanathan, K.; Harries, K.A. Acoustic emission monitoring of CFRP reinforced concrete slabs. *Constr. Build. Mater.* **2009**, *23*, 2016–2026, doi:10.1016/j.conbuildmat.2008.08.026.

26. Mustapha, S.; Lu, Y.; Li, J.; Ye, L. Damage detection in rebar-reinforced concrete beams based on time reversal of guided waves. *Struct. Heal. Monit.* **2014**, *13*, 347–358, doi:10.1177/1475921714521268.

27. Ramón, J.; Martínez-Ibernón, A.; Gandía-Romero, J.; Fraile, R.; Bataller, R.; Alcañiz, M.; García-Breijo, E.; Soto, J.; Zamora, J.R.; Martínez, A.; et al. Characterization of electrochemical systems using potential step voltammetry. Part I: Modeling by means of equivalent circuits. *Electrochim. Acta* **2019**, *323*, 134702, doi:10.1016/j.electacta.2019.134702.

28. Martínez-Ibernón, A.; Ramón, J.; Gandía-Romero, J.; Gasch, I.; Valcuende, M.; Alcañiz, M.; Soto, J. Characterization of electro-chemical systems using potential step voltammetry. Part II: Modeling of reversible systems. *Electrochim. Acta* **2019**, *328*, 135111, doi:10.1016/j.electacta.2019.135111.

29. Ramón, J.; Gandía-Romero, J.; Bataller, R.; Alcañiz, M.; Valcuende, M.; Soto, J. Potential step voltammetry: An approach to corrosion rate measurement of reinforcements in concrete. *Cem. Concr. Compos.* **2020**, *110*, 103590, doi:10.1016/j.cemconcomp.2020.103590.

30. Alcañiz, M.; Bataller, R.; Gandía-Romero, J.M.; Ramón, J.E.; Soto, J.; Valcuende, M. Sensor, Red de Sensores, Método y Programa Informático Para Determinar la Corrosión en una Estructura de Hormigón Armado. Invention Patent No. ES2545669A1, WO2016177929A1, EP3293509A1, 19 January 2016.

31. Ramón, J.E. Sistema de Sensores Embebidos Para Monitorizar la Corrosión de Estructuras de Hormigón Armado. Fundamento, Metodología y Aplicaciones. Ph.D. Thesis, Universitat Politècnica de València, València, Spain, September 2018, doi:10.4995/Thesis/10251/111823.

32. Gandía-Romero, J.M.; Ramón, J.E.; Bataller, R.; Palací, D.G.; Valcuende, M.; Soto, J. Influence of the area and distance between electrodes on resistivity measurements of concrete. *Mater. Struct.* **2016**, *50*, doi:10.1617/s11527-016-0925-2.

33. Ministerio de Fomento, Instrucción de Hormigón Estructural EHE-08, Madrid, Spain, 2008. (in Spanish)

34. Lataste, J.; Behloul, M.; Breysse, D. Characterisation of fibres distribution in a steel fibre reinforced concrete with electrical resistivity measurements. *NDT E Int.* **2008**, *41*, 638–647, doi:10.1016/j.ndteint.2008.03.008.

35. Galao, O.; Bañón, L.; Baeza, F.J.; Carmona, J.; Garcés, P. Highly conductive carbon fiber reinforced concrete for icing prevention and curing. *Materials* **2016**, *9*, 281, doi:10.3390/ma9040281.

36. Elkey, W.; Sellevold, E.J. *Electrical Resistivity of Concrete*; Norwegian Road Research Laboratory: Oslo, Norway, 1995; pp. 11–13.